

# Suppressing the Background Process to QED Compton Scattering for Delineating the Photon Content of the Proton

A. Mukherjee\* and C. Pisano†

*Institut für Physik, Universität Dortmund, D 44221 Dortmund, Germany*

(Dated: February 1, 2008)

## Abstract

We investigate the QED Compton process (QEDCS) in  $ep \rightarrow e\gamma p$  and  $ep \rightarrow e\gamma X$ , together with the major background coming from the virtual Compton scattering (VCS), where the photon is emitted from the hadronic vertex. We suggest new kinematical constraints which suppress the VCS background and are furthermore suitable for the extraction of the equivalent photon content of the proton at the HERA collider. We show that the cross section, commonly expressed in terms of the proton structure functions, is reasonably well described by the equivalent photon approximation of the proton, also in the inelastic channel in the proposed kinematical region.

---

\*Electronic address: [asmita@physik.uni-dortmund.de](mailto:asmita@physik.uni-dortmund.de)

†Electronic address: [pisano@harpo.physik.uni-dortmund.de](mailto:pisano@harpo.physik.uni-dortmund.de)

## I. INTRODUCTION

QED Compton scattering (QEDCS) in the process  $ep \rightarrow e\gamma X$ , where  $X$  is a general hadronic system, has long been suggested [1, 2, 3] as a unique possibility to determine the photon content of the proton  $\gamma(x, Q^2)$ , evaluated in the equivalent photon approximation (EPA), which is a very convenient and efficient tool to calculate cross sections having photon induced subprocesses [4, 5, 6, 7, 8, 9]. Recently, the QED Compton process, depicted in Fig. 1, has been analyzed in [10] appropriate for measurements at HERA. The corresponding events have a distinctive experimental signature: they are characterized by an electron and a photon in the final state, with their transverse momenta almost balancing each other and with little or no hadronic activity at the detector. In order to extract  $\gamma(x, Q^2)$ , several kinematical constraints have been imposed which suppressed the major background contribution coming from the virtual Compton scattering (VCS), depicted in Fig. 2, and also reduced the contributions from initial and final state radiation effects [11] unrelated to QED Compton scattering. Although the cross section in the elastic channel,  $ep \rightarrow e\gamma p$ , is very accurately described by the equivalent photon approximation (EPA), substantial discrepancy was observed in the inelastic channel and it was concluded that the EPA does not give an accurate description of the process in this channel [10]. In our previous paper [12], we did an independent study of the QED Compton process, subject to the kinematical cuts of the HERA experiment, and confirmed this result. We also showed that a measurement in bins of the variable  $x_\gamma$  shows better agreement with the EPA than the corresponding measurements in bins of the leptonic variable  $x_l$  (for definitions, see section III).

The purpose of this paper is to calculate the VCS background process, to study its relevance and to suggest new cuts to be imposed on the cross section for a more accurate extraction of  $\gamma(x, Q^2)$ . We perform a detailed study of the full process  $ep \rightarrow e\gamma X$ , both in the elastic (when  $X$  is a proton) and inelastic channel, taking into account the VCS, whose cross section in the inelastic channel is estimated utilizing an effective parton distribution of the proton. In the elastic channel, to make a relative estimate of the VCS, we take the proton to be pointlike and replace the vertex by an effective vertex. We suggest new kinematical constraints to suppress the inelastic VCS background, which turns out to be important in the phase space domain of the HERA experiment. We also investigate the impact of these constraints on the QEDCS cross section. We show that in the phase space region suggested

by us and accessible at HERA, the EPA provides a reasonably good description of the QEDCS cross section, also in the inelastic channel.

The plan of the paper is as follows. In sections II and III, we present the cross section in the elastic and inelastic channel respectively. Numerical results are given in section IV. Summary and conclusions are presented in section V. The explicit form of the matrix elements are shown in Appendices A and B.

## II. ELASTIC CHANNEL

The cross section for the elastic process

$$e(l) + p(P) \rightarrow e(l') + p(P') + \gamma(k') \quad (1)$$

can be written as [12]

$$\sigma_{\text{el}}(S) = \frac{\alpha^3}{2(S - m^2)} \int \frac{d\hat{s}}{2\pi} dPS_2(l + P; l' + k', P') dPS_2(l + k; l', k') \overline{|M_{\text{el}}|^2}, \quad (2)$$

where we have defined the invariants

$$S = (P + l)^2, \quad \hat{s} = (l + k)^2, \quad t = k^2. \quad (3)$$

$k = P - P'$  is the momentum transfer between the initial and the final proton and  $k'$  is the momentum of the final state observed (real) photon. As in [12], we neglect the electron mass  $m_e$  everywhere except when it is necessary to avoid divergences in the formulae and take the proton to be massive,  $P^2 = P'^2 = m^2$ . The relevant Feynman diagrams for this process are shown in Fig. 1, with  $X$  being a proton and  $P_X \equiv P'$ .

The Lorentz invariant  $N$ -particle phase-space element is written as

$$dPS_N(P; P_1, \dots, P_N) = (2\pi)^4 \delta\left(P - \sum_{i=1}^N P_i\right) \prod_{i=1}^N \frac{d^3 P_i}{(2\pi)^3 2P_i^0}. \quad (4)$$

We also write

$$dPS_2(l + P; l' + k', P') = \frac{dt}{8\pi(S - m^2)} \quad (5)$$

and

$$dPS_2(l + k; l', k') = \frac{d\hat{t} d\varphi^*}{16\pi^2(\hat{s} - t)}. \quad (6)$$

Here  $\varphi^*$  is the azimuthal angle of the outgoing  $e - \gamma$  system in the  $e - \gamma$  center-of-mass frame and  $\hat{t} = (l - l')^2$ .

Substituting Eqs. (5) and (6) in Eq. (2) we get

$$\sigma_{\text{el}}(S) = \frac{\alpha^3}{8\pi(S - m^2)^2} \int_{m_e^2}^{(\sqrt{S}-m)^2} d\hat{s} \int_{t_{\min}}^{t_{\max}} dt \int_{\hat{t}_{\min}}^{\hat{t}_{\max}} d\hat{t} \int_0^{2\pi} d\varphi^* \frac{1}{(\hat{s} - t)} \overline{|M_{\text{el}}|^2}. \quad (7)$$

The limits of integrations in Eq. (7) follow from kinematics and are given explicitly by Eqs. (2.18) and (2.24) in [12]. However, as it will be discussed in section IV, we will impose additional kinematical cuts relevant to the experiment at HERA.

As already shown in [12]

$$\overline{|M_{\text{el}}^{QEDCS}|^2} = \frac{1}{t^2} T_{\mu\nu}(l, k; l', k') H_{\text{el}}^{\mu\nu}(P, P'), \quad (8)$$

where  $T_{\mu\nu}$  is the leptonic tensor given by Eq. (2.9) of [12] divided by  $e^4$ , with  $e$  denoting the electron charge.  $H_{\mu\nu}$  is the hadronic tensor:

$$H_{\text{el}}^{\mu\nu}(P, P') = [H_1(t)(2P - k)^\mu(2P - k)^\nu + H_2(t)(tg^{\mu\nu} - k^\mu k^\nu)], \quad (9)$$

with

$$H_1(t) = \frac{G_E^2(t) - (t/4m^2) G_M^2(t)}{1 - t/4m^2}, \quad H_2(t) = G_M^2(t). \quad (10)$$

The electric and magnetic form factors can be expressed as a combination of the real form factors  $F_1(t)$ ,  $F_2(t)$ :

$$G_E(t) = F_1(t) - \tau F_2(t); \quad G_M(t) = F_1(t) + F_2(t), \quad \tau = -t/4m^2, \quad (11)$$

and they are empirically parametrized as dipoles:

$$G_E(t) = \frac{1}{[1 - t/(0.71 \text{ GeV}^2)]^2}, \quad G_M(t) = 2.79 G_E(t). \quad (12)$$

The full cross section for the process given by Eq. (7) also receives a contribution from the VCS in Fig. 2. The cross section for this process can be expressed in terms of off-forward or generalized parton distributions [13]. In addition, there are contributions due to the interference between the QEDCS and VCS. In order to make a numerical estimate of these effects, one needs some realistic parametrization of the off-forward distributions. Our aim is to estimate the VCS background so as to find the kinematical cuts necessary to suppress

it. We make a simplified approximation to calculate the VCS cross section. We take the proton to be a massive pointlike fermion, with the equivalent  $\gamma^*p$  vertex described by a factor  $-i\gamma^\mu F_1(t)$ . Incorporating the background effects, the cross section of the process in Eq. (1) is given by Eq.(7), where  $\overline{|M_{\text{el}}|^2}$  now becomes

$$\overline{|M_{\text{el}}|^2} = \overline{|M_{\text{el}}^{\text{QEDCS}}|^2} + \overline{|M_{\text{el}}^{\text{VCS}}|^2} - 2 \Re e \overline{M_{\text{el}}^{\text{QEDCS}} M_{\text{el}}^{\text{VCS}*}}. \quad (13)$$

The interference term will have opposite sign if we consider a positron instead of an electron. The explicit expressions of  $\overline{|M_{\text{el}}^{\text{QEDCS}}|^2}$ ,  $\overline{|M_{\text{el}}^{\text{VCS}}|^2}$  and  $2 \Re e \overline{M_{\text{el}}^{\text{QEDCS}} M_{\text{el}}^{\text{VCS}*}}$  are given in appendix A. The effect of proton mass is small in the kinematical range of HERA.

### III. INELASTIC CHANNEL

We next consider the corresponding inelastic process, where an electron and a photon are produced in the final state together with a general hadronic system  $X$ :

$$e(l) + p(P) \rightarrow e(l') + \gamma(k') + X(P_X), \quad (14)$$

with  $P_X = \sum_{X_i} P_{X_i}$  being the sum over all momenta of the hadronic system  $X$ . The exact calculation of the QEDCS rates follows our treatment in [12] based on the ALLM97 parametrization [14] of the proton structure function  $F_2(x_B, Q^2)$ .

For the purpose of evaluating the relative importance of the VCS background we resorted to a unified parton model estimate of the VCS and QEDCS rates. The cross section within the parton model is given by

$$\frac{d\sigma_{\text{inel}}}{dx_B dQ^2 d\hat{s} d\hat{t} d\varphi^*} = \sum_q q(x_B, Q^2) \frac{d\hat{\sigma}^q}{d\hat{s} dQ^2 d\hat{t} d\varphi^*}, \quad (15)$$

where  $q(x_B, Q^2)$  are the quark and antiquark distributions of the initial proton,  $q = u, d, s, \bar{u}, \bar{d}, \bar{s}$ . Furthermore,  $Q^2 = -k^2 = -(l' + k' - l)^2$ ,  $x_B = \frac{Q^2}{2P \cdot (-k)}$  and  $d\hat{\sigma}^q$  is the differential cross section of the subprocess

$$e(l) + q(p) \rightarrow e(l') + \gamma(k') + q(p'). \quad (16)$$

The relevant integrated cross section is given by

$$\begin{aligned} \sigma_{\text{inel}}(S) = & \frac{\alpha^3}{8\pi(S - m^2)^2} \sum_q \int_{W_{\min}^2}^{W_{\max}^2} dW^2 \int_{m_e^2}^{(\sqrt{S}-W)^2} d\hat{s} \int_{Q_{\min}^2}^{Q_{\max}^2} \frac{dQ^2}{Q^2} \int_{\hat{t}_{\min}}^{\hat{t}_{\max}} d\hat{t} \int_0^{2\pi} d\varphi^* \frac{1}{(\hat{s} + Q^2)} \\ & \times \overline{|M_{\text{inel}}|^2} q(x_B, Q^2), \end{aligned} \quad (17)$$

with  $W^2 = (p - k)^2 = m^2 + Q^2(1 - x_B)/x_B$ . The limits of integration are given explicitly by Eqs. (2.18), (3.11) and (3.12) of [12] with  $\hat{s}_{min} = m_e^2$ . Further constraints, related to the HERA kinematics, will be discussed in the numerical section. Similar to the elastic channel, we have

$$|\overline{M_{inel}}|^2 = |\overline{M_{inel}^{QEDCS}}|^2 + |\overline{M_{inel}^{VCS}}|^2 - 2 \Re \overline{M_{inel}^{QEDCS} M_{inel}^{VCS*}}. \quad (18)$$

Again, the interference term will have opposite sign for a positron. The explicit expressions are given in Appendix B. They are also given in [15, 16] for a massless proton. We point out that the analytic expression of the QED Compton scattering cross section in the inelastic channel was already given in [12] in terms of the proton structure functions  $F_2(x_B, Q^2)$  and  $F_1(x_B, Q^2)$ .

Furthermore, we introduce the auxiliary invariants  $\hat{S} = (p' + k')^2$  and  $\hat{U} = (p' - k)^2$ , which can be written in terms of measurable quantities,

$$\hat{S} = \frac{\hat{t}(x_l - x_B)}{x_l}, \quad \hat{U} = \hat{t} - \hat{S} + Q^2, \quad (19)$$

with  $x_l = \frac{-\hat{t}}{2P \cdot (l - l')}$ . In addition to the leptonic variable  $x_l$  we define  $x_\gamma = \frac{l \cdot k}{P \cdot l}$ , which represents the fraction of the longitudinal momentum of the proton carried by the virtual photon [12]. In the limit of the EPA, both  $x_l$  and  $x_\gamma$  are the same and become equal to  $x = \frac{\hat{s}}{S}$ .

#### IV. NUMERICAL RESULTS

In this section we present our numerical results. In order to select the QEDCS events, certain kinematical constraints are imposed in the Monte Carlo studies in [10, 11]. We introduce the following lab frame variables: energy of the final electron  $E'_e$ , energy of the final photon  $E'_\gamma$ , polar angles of the outgoing electron and photon,  $\theta_e$  and  $\theta_\gamma$  respectively, and acoplanarity angle  $\phi$ , which is defined as  $\phi = |\pi - |\phi_\gamma - \phi_e||$ , where  $\phi_\gamma$  and  $\phi_e$  are the azimuthal angles of the outgoing photon and electron respectively ( $0 \leq \phi_\gamma, \phi_e \leq 2\pi$ ). The cuts are given in column A of Table I (from hereafter, they will be referred to as the set A). The energies of the incoming particles are:  $E_e = 27.5$  GeV (electron) and  $E_p = 820$  GeV (proton). So far the photon and the electron in the final state have been identified only in the backward part of the H1 detector at HERA. To select signals where there are no hadronic activities near the two electromagnetic clusters, the final hadronic state must not be found

above the polar angle  $\theta_h^{\max} = \pi/2$  [10]. Motivated by this experimental arrangement, we have identified  $\theta_h$  with the polar angle of the final quark  $q'$  in the subprocess  $eq \rightarrow e\gamma q'$ . It can be shown that  $\theta_h$  is given by

$$\cos \theta_h \equiv \cos \theta_{q'} = \frac{1}{E_{q'}}(x_B E_p - E_e - E'_e \cos \theta_e - E'_\gamma \cos \theta_\gamma) \quad (20)$$

and  $E_{q'} = x_B E_p + E_e - E'_e - E'_\gamma$  being the energy of the final parton. Here we have assumed that the final hadrons are emitted collinearly with the struck quark  $q'$ . For the elastic process  $\theta_h \equiv \theta_{p'}$ , the polar angle of the scattered proton, can be obtained by substituting  $x_B = 1$  in the above expression. Thus we impose the additional condition [10]

$$\theta_h < \pi/2 \quad (21)$$

on the cross section. However, no constraint on the hadronic final state was used in the cross section calculation presented in [10]. Inclusion of Eq. (21) reduces the QEDCS cross section by about 10%.

In the kinematical region defined by the constraints mentioned above, the contributions from the initial and final state radiation, unrelated to QED Compton scattering, are suppressed [1, 2, 3, 11]. Furthermore, we checked that the event rates related to the elastic VCS process and its interference with elastic QEDCS are negligible compared to the ones corresponding to pure elastic QEDCS. This is expected because the elastic QEDCS cross section is very much dominated by the small values of the variable  $-t$ , compared to  $-\hat{t}$ , see Eqs. (A1) and (A2). Such an observation is similar to that of [11], where the elastic DVCS background was calculated using a Regge model in different kinematical bins. Our estimate was done taking the proton to be pointlike with an effective vertex, as discussed in section II. We find that, in this approximation, the elastic QEDCS cross section differs from the actual one in [12] by about 3% within the range defined by the kinematical constraints.

Fig. 3 shows the total (elastic + inelastic) QEDCS cross section in  $x_l - Q_l^2$  bins with  $Q_l^2 = -\hat{t}$ , subject to the cuts of set A. For comparison we have also plotted the cross section without the cut on  $\theta_h$ , similar to our analysis in [12]. This additional constraint affects the result only in the inelastic channel.

We checked that the upper limit in Eq. (21) reduces the contribution from the inelastic VCS reaction. In order to calculate it, one needs a model for the parton distributions  $q(x_B, Q^2)$ . However, in the relevant kinematical region,  $Q^2$  can be very small and may

become close to zero, where the parton picture is not applicable. Therefore, in our estimate, we replace the parton distribution  $q(x_B, Q^2)$  by an effective parton distribution

$$\tilde{q}(x_B, Q^2) = \frac{Q^2}{Q^2 + a Q_0^2} q(x_B, Q^2 + Q_0^2), \quad (22)$$

where  $a = 1/4$  and  $Q_0^2 = 0.4 \text{ GeV}^2$  are two parameters and  $q(x_B, Q^2)$  is the NLO GRV98 [17] parton distribution.  $Q_0^2$  prevents the scale in the distribution to become too low. Eq. (22) is motivated by a similar form used in [14, 18] for the parametrization of the structure function  $F_2(x_B, Q^2)$  in the low  $Q^2$  region. It is clear that at high  $Q^2$ ,  $\tilde{q}(x_B, Q^2) \rightarrow q(x_B, Q^2)$ .

In this paper, we introduce a new set of cuts, which are given in the column B of Table I (and will be referred to as the set B) for a better extraction of the equivalent photon distribution of the proton as well as to suppress the VCS background. These cuts will be compared to the set A in the following. Instead of the constraint on the acoplanarity, namely  $\phi < \pi/4$ , where the upper limit is actually ambiguous, we impose  $\hat{s} > Q^2$ . The relevance of the cut  $\hat{S} \gtrsim \hat{s}$  can be seen from Fig. 4. This shows the cross sections of the QEDCS and VCS processes in the inelastic channel, calculated using Eq. (17) and subject to the kinematical limits of set B (except  $\hat{S} \gtrsim \hat{s}$ ), in bins of  $\hat{s} - \hat{S}$ . Fig. 4 shows that the VCS cross section is higher than QEDCS for bins with  $\hat{s} \gtrsim \hat{S}$  but falls sharply in bins for which  $\hat{s}$  is close to  $\hat{S}$  and becomes much suppressed for  $\hat{S} \gtrsim \hat{s}$ . This is expected because  $\hat{S}$  corresponds to the quark propagator in the VCS cross section, see Eq. (B2), and a lower value enhances this contribution. In fact the sharp drop of the VCS cross section in bins where  $\hat{S} \gtrsim \hat{s}$  is due to the fact that both the propagators  $\hat{s}, \hat{u}$  in the QEDCS cross section are constrained to be smaller than  $\hat{S}, \hat{U}$  for VCS in these bins, see Eqs. (B1), (B2). The QEDCS cross section is always enhanced by the factor  $Q^2$  in the denominator of Eq. (B1) coming from the virtual photon, which can be very small in the kinematical region of interest here. This plot shows that imposing a cut on  $\hat{S}$  can be very effective in reducing the background contribution from VCS. The interference between inelastic QEDCS and VCS gives negligible contribution. We have also shown the QEDCS cross section using the ALLM97 parametrization of  $F_2(x_B, Q^2)$  [12]. The discrepancy between this and the one calculated using the parametrization in Eq. (22) is less than 5% in almost all the bins, and maximally 7% in two bins.

In Fig. 5(a), we have shown the inelastic QEDCS and VCS cross sections in bins of  $x_\gamma$ , subject to the cuts of set A. The VCS cross section is much suppressed in the smaller  $x_\gamma$  bins



but becomes enhanced as  $x_\gamma$  increases, which indicates that such a set of cuts is not suitable to remove the background at higher  $x_\gamma$ . The situation will be the same in  $x_l$  bins. Fig. 5(b) shows the cross sections but with the set B. The background in this case is suppressed for all  $x_\gamma$  bins, which means that such a cut is more effective in extracting QEDCS events also for higher  $x_\gamma$ . In addition, we have plotted the QEDCS cross section in terms of the structure function  $F_2(x_B, Q^2)$ , using the ALLM97 parametrization. Fig. 5 shows that our parametrization gives a reasonably good description of the proton, at least for the QEDCS process, in most of the bins except those with high  $x_\gamma$ . However, this parametrization has been used only to make a relative estimate of the background events. In fact, a quantitative estimate of the inelastic VCS events has not been presented in [10, 11].

Figs. 6(a) and 6(b) show the QEDCS cross section in bins of  $x_l$  and  $x_\gamma$ , respectively, subject to the constraints of set B. The elastic cross section has been calculated using Eqs. (7)-(12), as in [12]. The inelastic cross section is given by Eq. (3.10) of [12] in terms of the structure functions  $F_1(x_B, Q^2)$  and  $F_2(x_B, Q^2)$ . We have assumed the Callan-Gross relation and used the ALLM97 parametrization [14] for  $F_2(x_B, Q^2)$ . In this way the results presented in Fig. 6, labelled as 'exact', are free from the parton model approximations in Figs. 4 and 5. In the same plot, we have also shown the total cross section calculated in terms of the EPA, according to Eqs. (2.28) and (3.13) in [12]. Fig. 6(b) shows much better agreement between the approximate cross section based on the EPA and the 'exact' one. For Fig. 6(a), the discrepancy is about 3 – 7% in the first three bins, between 20 – 30% in three other bins and higher in the last bin. In Fig. 6(b) it is 1 – 6% in five bins, 13 – 15% in two bins and about 25% in the last bin. The discrepancy of the 'exact' cross section, integrated over  $x_\gamma$ , with the approximate one, when subject to the constraints of set B is 0.38% in the elastic channel and 4.5% in the inelastic one. The total (elastic + inelastic) discrepancy turns out to be 2.26%, which should be compared to the values 14%, already observed in [12] when subject to the set A, except the one on  $\theta_h$ , and 24% when this one is imposed too.

As we know, the elastic QEDCS cross section is described very accurately by the EPA [11, 12]. It is thus more interesting to investigate the inelastic channel in this context. The elastic QEDCS events can be separated from the inelastic ones by applying a cut on  $\theta_h$ . We have found that, with the restriction  $\theta_h \geq 0.1^\circ$ , the elastic events are rejected and all the inelastic events are retained in the cross section. A lower limit on  $\theta_h$  higher than  $1^\circ$  removes a substantial part (more than 30%) of the inelastic events.

Table II shows the 'exact' inelastic QEDCS cross section in  $x_l$  and  $Q_l^2$  bins, subject to the cuts A. We have also shown the cross section in the EPA with the same constraints (the last two cuts of set A are not relevant in this case). The discrepancy with the EPA is quite substantial. We have also shown the results with the cuts B, both the 'exact' and the one in terms of the EPA, in the same table (the constraint  $\hat{s} > Q^2$  is not relevant for the EPA). The discrepancy between the 'exact' and the EPA here is much less and on the average it is 20%. Table III is almost similar, the only difference is that the bins are now in  $x_\gamma$ . With the cuts of set A, the discrepancy now is on the average 50%, whereas, with the cuts B, the average discrepancy is 17%.

Our results show that the extraction of the equivalent photon distribution  $\gamma(x, Q^2)$  is very much dependent on the kinematical constraints utilized to single out QEDCS events, in particular on the one on acoplanarity. The kinematical limits presented here are much more appropriate than those suggested in [11] for a reliable extraction of  $\gamma(x, Q^2)$ . It is also clear that this discrepancy is entirely due to the inelastic channel, which was also observed in [11, 12].

## V. SUMMARY AND CONCLUSIONS

To summarize, in this paper we have analyzed the QED Compton process, relevant for the experimental determination of the equivalent photon distribution of the proton  $\gamma(x, Q^2)$ . We have also calculated the major background process, namely virtual Compton scattering, assuming an effective parametrization of the parton distributions of the proton, both in the elastic and inelastic channels. The elastic VCS is suppressed compared to the QEDCS, in the phase space region accessible at HERA. We have shown that a constraint on the invariants  $\hat{S} \gtrsim \hat{s}$  is very effective in removing the inelastic VCS background. Furthermore, the selection of the QEDCS events in the process  $ep \rightarrow e\gamma X$  is sensitive to the specific kinematical limits, in particular to the upper limit of the acoplanarity angle  $\phi$ , which was used in the recent analysis [10, 11] of events as observed with the HERA-H1 detector. Instead of the acoplanarity, one can also directly impose cuts on the invariants, like  $\hat{s} > Q^2$  (both of them are measurable quantities), which directly restricts one to the range of validity of the EPA. With these constraints, the total (elastic + inelastic) cross section agrees with the EPA within 3%. Thus, we conclude that by choosing the kinematical domain relevant for

this approximation carefully, it is possible to have a more accurate extraction of  $\gamma(x, Q^2)$ . This will also give the region of validity of the EPA, which is important to have a convenient and reliable estimate of the photon induced subprocesses in  $ep$  and  $pp$  colliders.

## VI. ACKNOWLEDGEMENTS

We warmly acknowledge E. Reya and M. Glück for initiating this study, as well as for many helpful discussions and suggestions. We also thank W. Vogelsang and V. Lendermann for helpful discussions. This work has been supported in part by the 'Bundesministerium für Bildung und Forschung', Berlin/Bonn.

## APPENDIX A: MATRIX ELEMENT FOR THE ELASTIC PROCESS

In this Appendix, we give the expressions of  $\overline{|M_{\text{el}}^{QEDCS}|^2}$ ,  $\overline{|M_{\text{el}}^{VCS}|^2}$  and  $2\Re \overline{M_{\text{el}}^{QEDCS}} M_{\text{el}}^{VCS*}$  corresponding to Eq. (7):

$$\overline{|M_{\text{el}}^{QEDCS}|^2} = \frac{4}{t \hat{s} \hat{u}} \left[ A + \frac{2m^2}{t} B \right] F_1^2(t), \quad (\text{A1})$$

$$\overline{|M_{\text{el}}^{VCS}|^2} = \frac{4}{\hat{t} U' \hat{S}'} \left[ A - \frac{2m^2}{\hat{t} U' \hat{S}'} C \right] F_1^2(\hat{t}), \quad (\text{A2})$$

with  $\hat{S} = -(\hat{s} + \hat{u} + U' - m^2)$ ,  $\hat{S}' = \hat{S} - m^2$  and

$$\begin{aligned} A = & 2 t^2 - 2 t (\hat{s} - 2 S' - U') + \hat{s}^2 - 2 \hat{s} S' \\ & + 4 S'^2 + 2 S' \hat{u} + \hat{u}^2 + 4 S' U' + 2 \hat{u} U' + 2 U'^2, \end{aligned} \quad (\text{A3})$$

$$B = 2 t^2 - 2 t (\hat{s} + \hat{u}) + \hat{s}^2 + \hat{u}^2, \quad (\text{A4})$$

$$\begin{aligned} C = & (\hat{s} + \hat{u})^2 [t^2 + \hat{s}^2 - 2 t (\hat{s} - S') - 2 \hat{s} S' \\ & + 2 S'^2 + 2 S' \hat{u} + \hat{u}^2 - 2 m^2 (\hat{s} + \hat{u} - t)] \\ & + 2 (\hat{s} + \hat{u}) [t^2 - t \hat{s} + \hat{u} (-\hat{s} + 2 S' + \hat{u})] U' \\ & + 2 [t^2 + \hat{u}^2 - t (\hat{s} + \hat{u})] U'^2. \end{aligned} \quad (\text{A5})$$

We have introduced the invariants  $U = (P - k')^2$ ,  $\hat{u} = (l - k')^2$  and used the notations  $S' = S - m^2$ ,  $U' = U - m^2$  for compactness.

For the interference between QEDCS and VCS we have

$$2 \Re \overline{M_{\text{el}}^{QEDCS}} M_{\text{el}}^{VCS*} = 4 \frac{D + 2m^2 E}{t \hat{s} \hat{u} \hat{t} U' \hat{S}'} F_1(\hat{t}) F_1(t), \quad (\text{A6})$$

with

$$\begin{aligned} D = & \{(\hat{s} + \hat{u}) [t \hat{u} + S' (\hat{s} + \hat{u})] + [\hat{s} (\hat{s} + \hat{u}) - t (\hat{s} - \hat{u})] U'\} \\ & [2 t^2 + \hat{s}^2 - 2 \hat{s} S' + 4 S'^2 + 2 S' \hat{u} + \hat{u}^2 - 2 t (\hat{s} - 2 S' - U') \\ & + 4 S' U' + 2 \hat{u} U' + 2 U'^2], \end{aligned} \quad (\text{A7})$$

$$\begin{aligned} E = & -S' \hat{u}^3 - \hat{s}^3 (S' - 2 \hat{u} + U') - \hat{s}^2 \hat{u} (7 S' + 2 U') - \hat{s} \hat{u}^2 (7 S' + 2 \hat{u} + 5 U') \\ & + 2 t^2 [\hat{s} (\hat{u} - U') + \hat{u} (\hat{u} + U')] - t (\hat{s} + \hat{u}) [\hat{s} (-2 S' + 3 \hat{u} - 3 U') \\ & + \hat{u} (-2 S' + \hat{u} + U')]. \end{aligned} \quad (\text{A8})$$

## APPENDIX B: MATRIX ELEMENT FOR THE INELASTIC PROCESS

Here we give the expressions of  $|\overline{M_{\text{inel}}^{QEDCS}}|^2$ ,  $|\overline{M_{\text{inel}}^{VCS}}|^2$  and  $2 \Re \overline{M_{\text{inel}}^{QEDCS}} M_{\text{inel}}^{VCS*}$  corresponding to Eq. (17):

$$|\overline{M_{\text{inel}}^{QEDCS}}|^2 = -4 e_q^2 \frac{F}{Q^2 \hat{s} \hat{u}}, \quad (\text{B1})$$

$$|\overline{M_{\text{inel}}^{VCS}}|^2 = 4 e_q^4 \frac{F}{\hat{t} \hat{U} \hat{S}}, \quad (\text{B2})$$

with  $\hat{S} = -(\hat{s} + \hat{u} + x_B U')$ ,  $\hat{U} = x_B U'$  and

$$\begin{aligned} F = & \hat{s}^2 + \hat{u}^2 + 2 \{Q^4 + Q^2 [\hat{s} - (2 S' + U') x_B] + x_B (S' \hat{u} + \hat{u} U' \\ & - \hat{s} S') + x_B^2 (2 S'^2 + 2 S' U' + U'^2)\}. \end{aligned} \quad (\text{B3})$$

Here  $e_q$  is the charge of the parton in units of the charge of the proton. Also we have

$$2 \Re \overline{M_{\text{inel}}^{QEDCS}} M_{\text{inel}}^{VCS*} = -4 e_q^3 \frac{G}{Q^2 \hat{s} \hat{u} \hat{t} \hat{U} \hat{S}} \quad (\text{B4})$$

with

$$\begin{aligned}
G = & \{-Q^2 \hat{u} (\hat{s} + \hat{u}) + Q^2 (\hat{s} - \hat{u}) U' x_B + (\hat{s} + \hat{u}) [S' \hat{u} \\
& + \hat{s} (S' + U')] x_B\} \{2 Q^4 + \hat{s}^2 + \hat{u}^2 - 2 \hat{s} S' x_B + 2 Q^2 [\hat{s} - (2 S' \\
& + U') x_B] + 2 x_B [\hat{u} (S' + U') + (2 S'^2 + 2 S' U' + U'^2) x_B]\}. \quad (\text{B5})
\end{aligned}$$

The analytic form of the interference term agrees with [15] but differs from [16] in the massless case slightly, in particular in Eq. (15) of [16], 8 in the first line should be replaced by 4 and  $(-8)$  in the sixth line should be replaced by  $(-16)$ . However we have checked that this does not affect our numerical results for HERA kinematics.

- 
- [1] A. Courau and P. Kessler, Phys. Rev. **D 46**, 117, (1992).
  - [2] J. Blümlein, G. Levman, H. Spiesberger, J. Phys. **G 19**, 1695 (1993).
  - [3] A. De Rujula, W. Vogelsang, Phys. Lett. **B 451** 437 (1999).
  - [4] B. Kniehl, Phys. Lett. **B 254**, 267, (1991).
  - [5] M. Drees, R. M. Godbole, M. Nowakowski, S. Rindani, Phys. Rev. **D 50**, 2335 (1994).
  - [6] J. Ohnemus, T. F. Walsh, P. M. Zerwas, Phys. Lett. **B 328**, 369 (1994).
  - [7] M. Glück, M. Stratmann, W. Vogelsang, Phys. Lett. **B 343**, 399 (1995).
  - [8] M. Glück, C. Pisano, E. Reya, Phys. Lett. **B 540**, 75, (2002).
  - [9] M. Glück, C. Pisano, E. Reya, I. Schienbein, Eur. Phys. J. **C 27**, 427 (2003).
  - [10] V. Lendermann, H. C. Schultz-Coulon, D. Wegener, Eur. Phys. Jour. **C 31** 343 (2003).
  - [11] V. Lenderman, Ph. D. thesis, Univ. Dortmund, H1 collaboration, DESY-THESIS-2002-004, (2002).
  - [12] A. Mukherjee and C. Pisano, Eur. Phys. J. **C 30**, 477 (2003).
  - [13] X. Ji, Phys. Rev. **D 55**, 7114 (1997).
  - [14] H. Abramowicz and A. Levy, hep-ph/9712415.
  - [15] S. J. Brodsky, J. F. Gunion, R. Jaffe, Phys. Rev. **D 6**, 2487 (1972).
  - [16] P. Hoyer, M. Maul and A. Metz, Eur. Phys. J. **C 17**, 113 (2000).
  - [17] M. Glück, E. Reya, A. Vogt, Eur. Phys. J. **C 5**, 461 (1998).
  - [18] B. Badelek and J. Kwiecinski, Phys. Lett. **B 295**, 263 (1992).

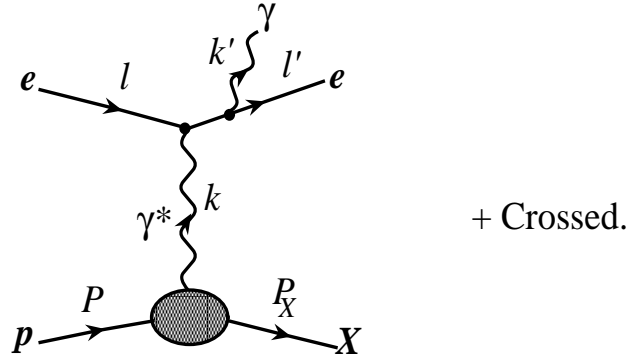


Fig. 1: Feynman diagrams for the QED Compton process (QEDCS).  $X \equiv p$  (and  $P_X \equiv P'$ ) corresponds to elastic scattering.

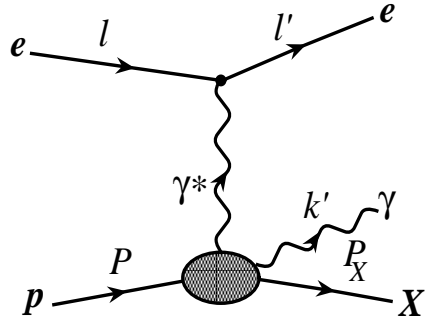


Fig. 2: As in Fig. 1 but for the virtual Compton scattering (VCS) background process.

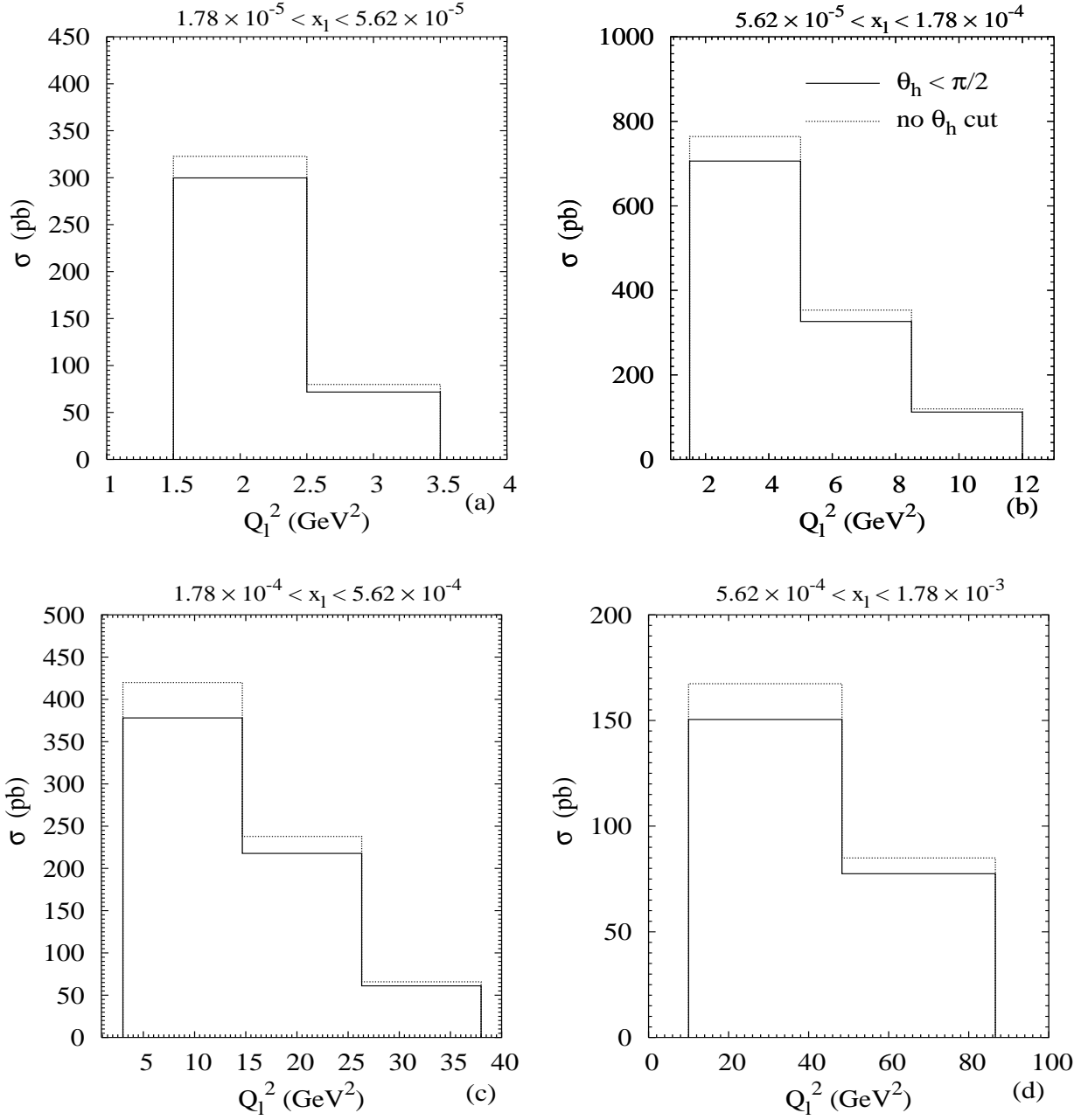


Fig. 3: Double differential cross section for QED Compton scattering at HERA-H1. The kinematical bins correspond to Table 1 of [12]. The continuous line describes the total (elastic + inelastic) cross section subject to the set of cuts A in table I. The dotted line shows the same results when the constraint on  $\theta_h$  is removed.

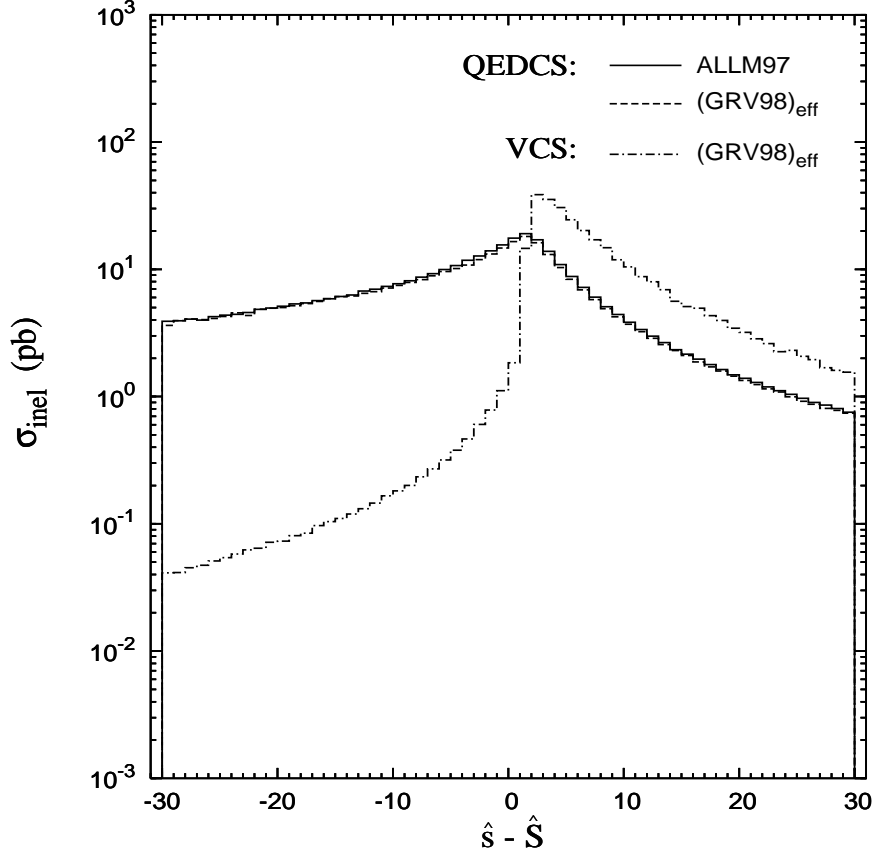


Fig. 4: Cross section for the QEDCS and VCS processes (inelastic) at HERA-H1. The bins are in  $\hat{s} - \hat{S}$ , expressed in  $\text{GeV}^2$ . The cuts applied are listed in table I, set B (except  $\hat{S} \gtrsim \hat{s}$ ). The continuous line corresponds to the QEDCS cross section with ALLM97 parametrization of  $F_2(x_B, Q^2)$ , the dashed line corresponds to the QEDCS cross section using the effective GRV98 parton distributions in Eq. (22) and the dashed dotted line corresponds to the VCS cross section using the same effective distributions.



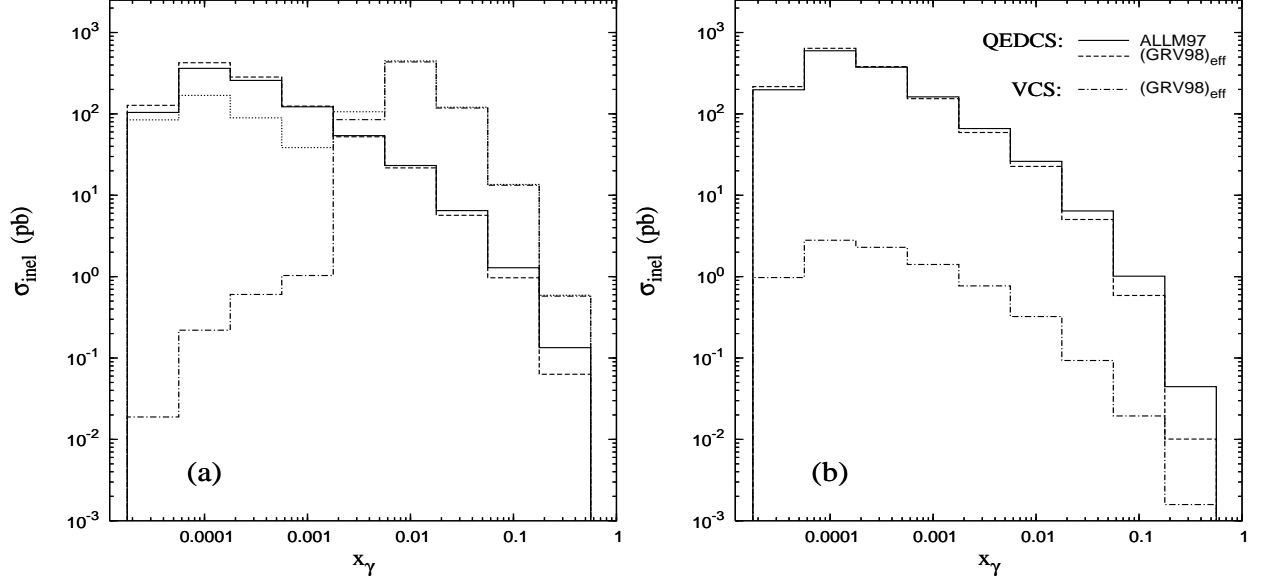


Fig. 5: Cross section for QED Compton scattering in bins of  $x_\gamma$  as calculated with the ALLM97 (full line) and the  $(\text{GRV98})_{\text{eff}}$  (dashed line) parametrization of  $F_2(x_B, Q^2)$ , respectively, as compared to the VCS background cross section (dot-dashed line). The cuts employed are: a) as in set A, b) as in set B of table I. The dotted line in Fig. 5 a) shows the VCS cross section subject to the set of cuts A without the constraint on  $\theta_h$ .

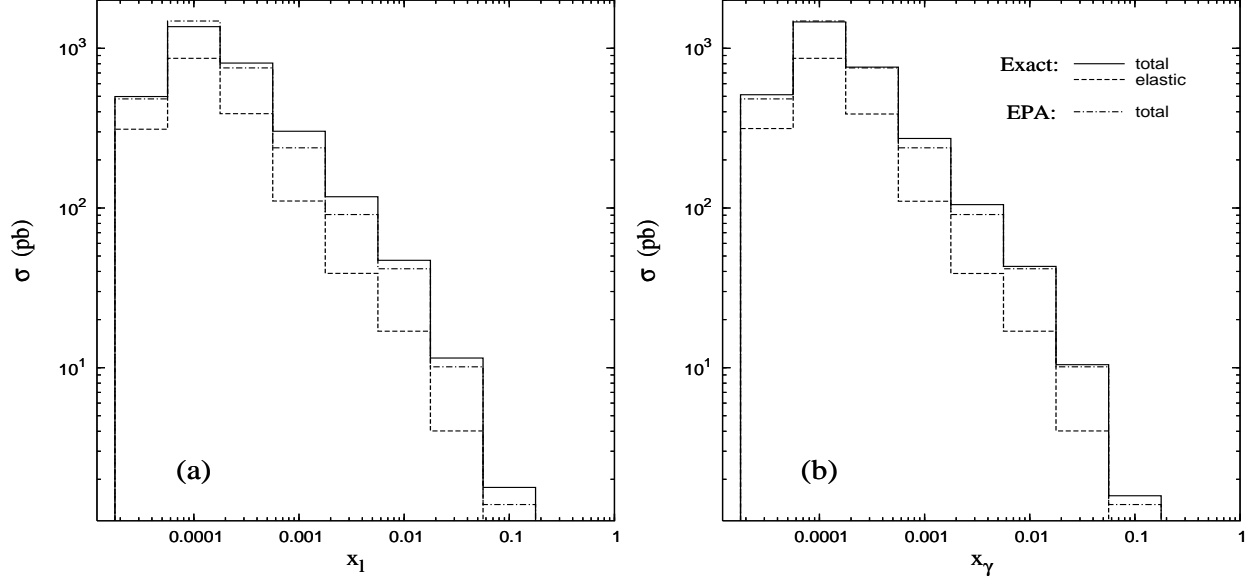


Fig. 6: Cross section for QED Compton scattering at HERA-H1 subject to the cuts of set B in table I, in (a)  $x_l$  bins, (b)  $x_\gamma$  bins. The continuous line corresponds to our exact calculation using ALLM97 parametrization of  $F_2(x_B, Q^2)$ , the dot-dashed line corresponds to the same in the EPA, the dashed line shows the elastic contribution.

$A$	$B$
$E'_e, E'_\gamma > 4 \text{ GeV}$ $E'_e + E'_\gamma > 20 \text{ GeV}$ $0.06 < \theta_e, \theta_\gamma < \pi - 0.06$ $\phi < \pi/4$ $\theta_h < \pi/2$	$E'_e, E'_\gamma > 4 \text{ GeV}$ $E'_e + E'_\gamma > 20 \text{ GeV}$ $0.06 < \theta_e, \theta_\gamma < \pi - 0.06$ $\hat{s} > Q^2$ $\hat{S} > \hat{s}$

TABLE I: A: cuts to simulate HERA-H1 detector. B: cuts introduced in this paper.

$x_l$ bin	$Q_l^2$ bin	$\sigma_{\text{inel}}$	$\sigma_{\text{inel}}^{\text{EPA}}$	$\sigma_{\text{inel}}^*$	$\sigma_{\text{inel}}^{\text{EPA}*}$
$1.78 \times 10^{-5} - 5.62 \times 10^{-5}$	1.5 – 2.5	$5.697 \times 10^1$	$1.529 \times 10^2$	$1.097 \times 10^2$	$1.344 \times 10^2$
$1.78 \times 10^{-5} - 5.62 \times 10^{-5}$	2.5 – 3.5	$2.074 \times 10^1$	$3.362 \times 10^1$	$4.067 \times 10^1$	$2.994 \times 10^1$
$5.62 \times 10^{-5} - 1.78 \times 10^{-4}$	1.5 – 5.0	$1.781 \times 10^2$	$4.116 \times 10^2$	$3.050 \times 10^2$	$3.518 \times 10^2$
$5.62 \times 10^{-5} - 1.78 \times 10^{-4}$	5.0 – 8.5	$8.681 \times 10^1$	$2.098 \times 10^2$	$1.467 \times 10^2$	$1.847 \times 10^2$
$5.62 \times 10^{-5} - 1.78 \times 10^{-4}$	8.5 – 12.0	$2.713 \times 10^1$	$8.091 \times 10^1$	$4.523 \times 10^1$	$7.223 \times 10^1$
$1.78 \times 10^{-4} - 5.62 \times 10^{-4}$	3.0 – 14.67	$1.701 \times 10^2$	$2.210 \times 10^2$	$2.464 \times 10^2$	$1.826 \times 10^2$
$1.78 \times 10^{-4} - 5.62 \times 10^{-4}$	14.67 – 26.33	$8.057 \times 10^1$	$1.557 \times 10^2$	$1.264 \times 10^2$	$1.363 \times 10^2$
$1.78 \times 10^{-4} - 5.62 \times 10^{-4}$	26.33 – 38.0	$2.396 \times 10^1$	$4.558 \times 10^1$	$3.778 \times 10^1$	$4.017 \times 10^1$
$5.62 \times 10^{-4} - 1.78 \times 10^{-3}$	10.0 – 48.33	$9.102 \times 10^1$	$8.092 \times 10^1$	$1.081 \times 10^2$	$6.516 \times 10^1$
$5.62 \times 10^{-4} - 1.78 \times 10^{-3}$	48.33 – 86.67	$4.036 \times 10^1$	$5.272 \times 10^1$	$6.137 \times 10^1$	$4.541 \times 10^1$
$5.62 \times 10^{-4} - 1.78 \times 10^{-3}$	86.67 – 125.0	$1.154 \times 10^1$	$1.587 \times 10^1$	$1.803 \times 10^1$	$1.378 \times 10^1$
$1.78 \times 10^{-3} - 5.62 \times 10^{-3}$	22 – 168	$4.282 \times 10^1$	$3.080 \times 10^1$	$4.272 \times 10^1$	$2.390 \times 10^1$
$1.78 \times 10^{-3} - 5.62 \times 10^{-3}$	168 – 314	$1.800 \times 10^1$	$2.059 \times 10^1$	$2.599 \times 10^1$	$1.752 \times 10^1$
$1.78 \times 10^{-3} - 5.62 \times 10^{-3}$	314 – 460	6.467	$1.021 \times 10^1$	8.928	8.804
$5.62 \times 10^{-3} - 1.78 \times 10^{-2}$	0 – 500	$1.406 \times 10^1$	8.823	$1.133 \times 10^1$	6.048
$5.62 \times 10^{-3} - 1.78 \times 10^{-2}$	500 – 1000	$1.151 \times 10^1$	$1.687 \times 10^1$	$1.484 \times 10^1$	$1.425 \times 10^1$
$5.62 \times 10^{-3} - 1.78 \times 10^{-2}$	1000 – 1500	2.985	4.885	3.708	4.090
$1.78 \times 10^{-2} - 5.62 \times 10^{-2}$	0 – 1500	3.506	1.811	2.200	1.030
$1.78 \times 10^{-2} - 5.62 \times 10^{-2}$	1500 – 3000	3.621	4.867	4.139	3.908
$1.78 \times 10^{-2} - 5.62 \times 10^{-2}$	3000 – 4500	$9.366 \times 10^{-1}$	1.341	1.028	1.044
$5.62 \times 10^{-2} - 1.78 \times 10^{-1}$	10 – 6005	1.079	$7.147 \times 10^{-1}$	$6.723 \times 10^{-1}$	$3.990 \times 10^{-1}$
$5.62 \times 10^{-2} - 1.78 \times 10^{-1}$	6005 – 12000	$5.382 \times 10^{-1}$	$5.922 \times 10^{-1}$	$4.953 \times 10^{-1}$	$3.890 \times 10^{-1}$
$5.62 \times 10^{-2} - 1.78 \times 10^{-1}$	12000 – 17995	$6.035 \times 10^{-2}$	$6.789 \times 10^{-2}$	$4.613 \times 10^{-2}$	$3.662 \times 10^{-2}$

TABLE II: Double differential QED Compton scattering cross section (inelastic) in  $x_l$  and  $Q_l^2$  bins.

$\sigma_{\text{inel}}$  and  $\sigma_{\text{inel}}^*$  correspond to the 'exact' (without the EPA) cross section subject to the cuts A and B of Table I respectively.  $\sigma_{\text{inel}}^{\text{EPA}}$  and  $\sigma_{\text{inel}}^{\text{EPA}*}$  correspond to the one in the EPA and subject to the cuts A and B respectively.  $Q_l^2$  is expressed in  $\text{GeV}^2$  and the cross-sections are in pb.

$x_\gamma$ bin	$Q_l^2$ bin	$\sigma_{\text{inel}}$	$\sigma_{\text{inel}}^{\text{EPA}}$	$\sigma_{\text{inel}}^*$	$\sigma_{\text{inel}}^{\text{EPA}*}$
$1.78 \times 10^{-5} - 5.62 \times 10^{-5}$	1.5 – 2.5	$5.331 \times 10^1$	$1.529 \times 10^2$	$1.022 \times 10^2$	$1.344 \times 10^2$
$1.78 \times 10^{-5} - 5.62 \times 10^{-5}$	2.5 – 3.5	$2.957 \times 10^1$	$3.362 \times 10^1$	$5.368 \times 10^1$	$2.994 \times 10^1$
$5.62 \times 10^{-5} - 1.78 \times 10^{-4}$	1.5 – 5.0	$1.825 \times 10^2$	$4.116 \times 10^2$	$3.111 \times 10^2$	$3.518 \times 10^2$
$5.62 \times 10^{-5} - 1.78 \times 10^{-4}$	5.0 – 8.5	$1.151 \times 10^2$	$2.098 \times 10^2$	$1.856 \times 10^2$	$1.847 \times 10^2$
$5.62 \times 10^{-5} - 1.78 \times 10^{-4}$	8.5 – 12.0	$4.809 \times 10^1$	$8.091 \times 10^1$	$7.550 \times 10^1$	$7.223 \times 10^1$
$1.78 \times 10^{-4} - 5.62 \times 10^{-4}$	3.0 – 14.67	$1.056 \times 10^2$	$2.210 \times 10^2$	$1.523 \times 10^2$	$1.826 \times 10^2$
$1.78 \times 10^{-4} - 5.62 \times 10^{-4}$	14.67 – 26.33	$9.862 \times 10^1$	$1.557 \times 10^2$	$1.432 \times 10^2$	$1.363 \times 10^2$
$1.78 \times 10^{-4} - 5.62 \times 10^{-4}$	26.33 – 38.0	$3.819 \times 10^1$	$4.558 \times 10^1$	$5.539 \times 10^1$	$4.017 \times 10^1$
$5.62 \times 10^{-4} - 1.78 \times 10^{-3}$	10.0 – 48.33	$4.717 \times 10^1$	$8.092 \times 10^1$	$5.829 \times 10^1$	$6.516 \times 10^1$
$5.62 \times 10^{-4} - 1.78 \times 10^{-3}$	48.33 – 86.67	$4.865 \times 10^1$	$5.272 \times 10^1$	$6.648 \times 10^1$	$4.541 \times 10^1$
$5.62 \times 10^{-4} - 1.78 \times 10^{-3}$	86.67 – 125.0	$1.774 \times 10^1$	$1.587 \times 10^1$	$2.463 \times 10^1$	$1.378 \times 10^1$
$1.78 \times 10^{-3} - 5.62 \times 10^{-3}$	22 – 168	$2.222 \times 10^1$	$3.080 \times 10^1$	$2.452 \times 10^1$	$2.390 \times 10^1$
$1.78 \times 10^{-3} - 5.62 \times 10^{-3}$	168 – 314	$2.128 \times 10^1$	$2.059 \times 10^1$	$2.761 \times 10^1$	$1.752 \times 10^1$
$1.78 \times 10^{-3} - 5.62 \times 10^{-3}$	314 – 460	8.593	$1.021 \times 10^1$	$1.131 \times 10^1$	8.804
$5.62 \times 10^{-3} - 1.78 \times 10^{-2}$	0 – 500	6.944	8.823	6.344	6.048
$5.62 \times 10^{-3} - 1.78 \times 10^{-2}$	500 – 1000	$1.243 \times 10^1$	$1.687 \times 10^1$	$1.514 \times 10^1$	$1.425 \times 10^1$
$5.62 \times 10^{-3} - 1.78 \times 10^{-2}$	1000 – 1500	3.572	4.885	4.311	4.090
$1.78 \times 10^{-2} - 5.62 \times 10^{-2}$	0 – 1500	1.568	1.811	1.101	1.030
$1.78 \times 10^{-2} - 5.62 \times 10^{-2}$	1500 – 3000	3.720	4.867	4.052	3.908
$1.78 \times 10^{-2} - 5.62 \times 10^{-2}$	3000 – 4500	1.057	1.341	1.121	1.044
$5.62 \times 10^{-2} - 1.78 \times 10^{-1}$	10 – 6005	$6.448 \times 10^{-1}$	$7.147 \times 10^{-1}$	$4.548 \times 10^{-1}$	$3.990 \times 10^{-1}$
$5.62 \times 10^{-2} - 1.78 \times 10^{-1}$	6005 – 12000	$5.671 \times 10^{-1}$	$5.922 \times 10^{-1}$	$5.003 \times 10^{-1}$	$3.890 \times 10^{-1}$
$5.62 \times 10^{-2} - 1.78 \times 10^{-1}$	12000 – 17995	$7.343 \times 10^{-2}$	$6.789 \times 10^{-2}$	$5.664 \times 10^{-2}$	$3.662 \times 10^{-2}$

TABLE III: As in table II but for  $x_\gamma$  bins.